Novel device to study double-alpha decay at the FRS Ion Catcher

L Varga, H Wilsenach, O Hall, T Dickel, M.P Reiter, D Amanbayev, T Davinson, D.J Morrissey, I Pohjalainen, N Tortorelli, et al.

Nuclear Instruments and Methods in Physics Research A 1063 (2024) 169252

Contents lists available at ScienceDirect

Nuclear Inst. and Methods in Physics Research, A

journal homepage: www.elsevier.com/locate/nima

Full Length Article

Novel device to study double-alpha decay at the FRS Ion Catcher

L. Varga [a,b,*], H. Wilsenach [c,f], O. Hall [a], T. Dickel [b,c], M.P. Reiter [a], D. Amanbayev [c,l], T. Davinson [a], D.J. Morrissey [d], I. Pohjalainen [b], N. Tortorelli [b,e], J. Yu [b], J. Zhao [b], S. Ayet [h,b,a], S. Beck [b], J. Bergmann [c], Z. Ge [b], H. Geissel [b,c], L. Heitz [i,m], C. Hornung [b], N. Kalantar-Nayestanaki [j], E. Khan [m], G. Kripko-Koncz [c,l], I. Mardor [f,g], M. Narang [j,b], W. Plass [b,c], C. Scheidenberger [b,c,l], M. Simonov [c,l], S.K. Singh [b], A. State [k], C. Theisen [i,†], M. Vandebrouck [i], P.J. Woods [a], FRS Ion Catcher Collaboration

[a] School of Physics and Astronomy, University of Edinburgh, Edinburgh, EH9 3FD, UK
[b] GSI Helmholtzzentrum für Schwerionenforschung GmbH, 64291 Darmstadt, Germany
[c] II. Physikalisches Institut, Justus-Liebig-Universität Gießen, 35392 Gießen, Germany
[d] Department of Chemistry, Michigan State University, East Lansing, MI, 48824, USA
[e] Ludwig-Maximilians-Universität München, Germany
[f] School of Physics and Astronomy, Tel Aviv University, 6997801 Tel Aviv, Israel
[g] Soreq Nuclear Research Center, 81800 Yavne, Israel
[h] University Valencia, 46010 Valencia, Spain
[i] Irfu, CEA, Université Paris-Saclay, 91191 Gif-sur-Yvette, France
[j] Nuclear Energy Group, ESRIG, University of Groningen, Zernikelaan 25, 9747 AA, Groningen, The Netherlands
[k] Extreme Light Infrastructure-Nuclear Physics (ELI-NP), Horia Hulubei National Institute for R& D in Physics and Nuclear Engineering, Str. Reactorului 30, 077125 Bucharest-Măgurele, Romania
[l] Helmholtz Research Academy Hesse for FAIR (HFHF), GSI Helmholtz Center for Heavy Ion Research, Gießen, 35392, Germany
[m] IJCLab, Université Paris-Saclay, CNRS/IN2P3, 91405 Orsay Cedex, France

ARTICLE INFO

Keywords:
Double-alpha decay
224-Ra
Cryogenic stopping cell
DSSD
Exotic radioactive decay modes

ABSTRACT

A novel system has been developed to detect simultaneous double-alpha emission from purified and weightless sources. The system includes the collection of ^{224}Ra low-energy recoils in purified helium buffer gas from the decay of ^{228}Th. The recoil products are thermalized and collected in a cryogenic buffer gas cell and extracted into an RF-ion guide for mass selection. The mass-separated ions are implanted at low kinetic energy into a thin carbon foil placed between two large-area double-sided silicon strip detectors to observe correlated alpha-particle emission. The apparatus is described in detail, including insights into its experimental performance.

1. Introduction

Several nuclear decay processes have been observed with two particles of the same nature emitted simultaneously. For example, double gamma-ray emission [1,2] or double-beta decay in which two electrons are emitted along with two antineutrinos [3–5] are both well known. In addition, nuclear decays with simultaneous emission of two protons [6,7] and two neutrons [8] have been observed from nuclei close to the proton and neutron drip lines, respectively. Simultaneous double-alpha decay via the emission of a ^{8}Be nucleus was first studied in the mid-1980s [9], but has not been observed up to the present due to its small predicted branching ratio. By analyzing the data taken from the experiment conducted by Marcillac et al. [10], to observe single alpha decay from ^{209}Bi, Tretyak [11] set the experimental limit for double-alpha emission from ^{209}Bi as $T_{1/2} > 2.9 \times 10^{20}$ years. Since that time, two different decay modes have emerged. The first one is derived from theoretical frameworks describing the emission of a ^{8}Be cluster with subsequent rapid separation into two alpha particles [9,11]. Similar phenomenological theoretical calculations of two alpha emission have also been reported [12,13], with low branching ratios similar to those of [9]. Recently, a second decay mode has been predicted with the simultaneous emission of two alpha particles in opposite directions [14–16]. In the microscopic theoretical studies [14,16], the so-called back-to-back decay is favored by more than

* Corresponding author at: GSI Helmholtzzentrum für Schwerionenforschung GmbH, 64291 Darmstadt, Germany.
E-mail address: l.varga@gsi.de (L. Varga).
† Deceased author.

https://doi.org/10.1016/j.nima.2024.169252
Received 11 August 2023; Received in revised form 6 March 2024; Accepted 13 March 2024
Available online 27 March 2024

10 orders of magnitude compared to the ^{8}Be double-alpha decay mode. These calculations were carried out in the ^{224}Ra region and predicted branching ratios of 2.9×10^{-8} with respect to single alpha decay [16]. Such branching ratios are of the order of previously observed heavy-cluster emission from heavy nuclei [17,18] and should be accessible to sensitive measurements. Studies of the decay of ^{224}Ra are particularly attractive since this nucleus can be harvested from the alpha decay of the relatively long-lived parent ^{228}Th ($T_{1/2}$ = 1.9116(16) yr [19]) which is readily available in thin, open sources. ^{224}Ra has been found to predominantly decay via the emission of an alpha particle with a tiny ^{14}C decay branch [20]. The detection of two alpha particles with a 180° opening angle and equal kinetic energies in a single event provides a unique signature of the two-alpha decay and strong evidence of the novel decay with only a few events. In addition, the ^{220}Rn nucleus in the decay chain has also been predicted to have an observable double-alpha decay branch.

Here we report a new experimental setup at the FRS Ion Catcher at GSI Helmholtz center for heavy ion research in Germany [21]. The apparatus combines the collection of heavy recoiling nuclei in the Cryogenic Stopping Cell (CSC) [22] with a nearly 4π Double-sided Silicon Strip Detector (DSSD) system for charged particle detection. The experiment was performed with radioactive sources, as compared to an online radioactive beam, and thus continuous data-taking over a long period of four months was possible. The setup can be used to investigate also other rare decays in a quasi background free way. Other such rare decays include the emission of protons by nuclei close to the proton drip line [23–27] as well as beta delayed proton emission [28–30]. In addition, study of the two-neutrino double beta decay in ^{220}Rn and ^{216}Po should be possible. The present report focuses on the experimental technique for the double-alpha decay measurement with presentation of the observed hit, energy, and time spectra that highlight key elements of the background suppression.

2. General considerations for the design of the experiment

Recent theoretical investigations have identified ^{224}Ra as the most promising candidate to find the first case of a double alpha decay experimentally [14–16]. In the following, different aspects are presented to design the experiment with the highest sensitivity to discover the double-alpha decay. This section is focused on the production of ^{224}Ra ions by an alpha recoil source of ^{228}Th. A comparison is made to an accelerator-based production, concluding that an "offline" experiment with moderate source strength promises the best case scenario for the double-alpha decay search in ^{224}Ra.

2.1. Counting rate and decay chain

The goal is to observe a statistically significant number of coincident alpha decay events with the predicted energies, back-to-back angular correlation, and simultaneous time signature. A general expression for the counting rate of single alpha events from ^{224}Ra decay, R_1, and the total number of its single alpha events, N_1, would be:

$$R_1 = A_{\mathrm{Th}} \cdot \epsilon_{\mathrm{Coll}} \cdot \epsilon_{\mathrm{Trans}} \cdot \epsilon_{\mathrm{Det}} \cdot \mathrm{BR}_1 \quad (1)$$

$$N_1 = R_1 \cdot T_{\mathrm{Obs}} \quad (2)$$

where A_{Th} is the activity of the ^{228}Th source, ϵ_{Coll} is the total efficiency for collection of the recoiling ^{224}Ra ions and beam formation at the exit of the CSC, $\epsilon_{\mathrm{Trans}}$ is the total efficiency to transport ^{224}Ra ions to the implantation foil, and ϵ_{Det} is the total efficiency for detecting a single or double event, including dead-time, from the implanted ^{224}Ra. Since the branching ratio for single alpha emission, BR_1, is essentially one, and the back to back decay has a detection efficiency close to 100%, the number of double-alpha events, N_2, can be expressed as:

$$N_2 = N_1 \cdot \mathrm{BR}_2 \quad (3)$$

Table 1
The strongest alpha lines are listed in the^{228}Th decay chain and ranked by the kinetic energy of each alpha particle (highest energy is on the top) [31–34].

Daughter isotope	Alpha decay energy [keV]	Absolute intensity [%]
^{224}Ra	5685.37(15)	94.92(5)
	5448.6(12)	5.06(5)
^{220}Rn	6288.08(10)	99.886(17)
	5747	0.114(17)
^{216}Po	6778.3(5)	99.9981(3)
^{212}Bi	6089.88(3)	9.75(5)
	6050.78(3)	25.13(7)
	5768	0.6110
	5607	0.4061
^{212}Po	8784.86(12)	64

Table 2
The parameters in Eq. (1) are evaluated for conceivable estimates for offline experiments, for the values obtained in the present offline measurement, and for a scenario using an online radioactive beam at GSI. The random coincidence rate (R_{Coin}) is calculated for a time resolution of 20 ns. See the text for further details of the actual measurement.

Param.	Conceivable	Present	Online
A_{Th}	1 MBq	34 kBq	200 kBq
ϵ_{Coll}	0.45	0.45	0.5
$\epsilon_{\mathrm{Trans}}$	0.9	0.5	0.9
ϵ_{Det}	0.9	0.66	0.9
T_{Obs}	1 year	1 month	1 week
R_1	360 kBq	5.0 kBq	81 kBq
R_{Coin}	6.9×10^{-2} Bq	1.3×10^{-5} Bq	3.4×10^{-3} Bq
N_1	1.2×10^{13}	1.3×10^{10}	4.9×10^{10}
N_2	3.3×10^{5}	3.8×10^{2}	1.4×10^{3}
R_2	1.1×10^{-2} Bq	1.5×10^{-4} Bq	2.3×10^{-3} Bq

where BR_2 is the branching ratio of the double-alpha decay mode.

The sequential decay of nuclides from ^{224}Ra to ^{208}Pb with a variety of half-lives presents several challenges for the proposed measurement, see Table 1. For example, the ^{224}Ra half-life of 3.6316(23) d [31] is much longer than any of the five intermediate nuclei before reaching the stable final product ^{208}Pb and four of these intermediate nuclei emit alpha particles. Moreover, the child nuclei can effuse through the system due to the recoil energy they receive from the alpha decay. In addition to this, the first child nuclide ^{220}Rn, a noble gas with a 55.6(1) s half-life [31], can also effuse through the vacuum system. Both of these effects indicate that subsequent single alpha decays can occur at locations that are different from the main collection point. Table 2 contains a list of current estimates of the parameters in Eqs. (1) and (2) assuming back-to-back alpha emissions and conceivable values for future offline experiments. If one takes the latest theoretical estimate of the double-alpha branching ratio to be 2.9×10^{-8} [16], then the expected number of double events in the present experiment measured within one month would be in the order of $N_2 \sim 100$.

The strongest alpha lines for the ^{228}Th decay chain with the kinetic energy of each alpha particle [31–34] are listed in Table 1. The energy values of the alpha particles for the double alpha decays can be derived as the arithmetic mean of the Q-values from the two subsequent alpha decays of the mother nuclei and taken as $(\frac{1}{2}Q_{2\alpha})^{224Ra} = 6096.83(9)$ keV and $(\frac{1}{2}Q_{2\alpha})^{220Rn} = 6655.5(3)$ keV.

The region of interest was chosen to encompass as much of the signal as possible and was placed around the values of $(\frac{1}{2}Q_{2\alpha})$ of the decays. The signal in this region is thus expected to be the only real coincidence. The only background considered originates from random events, in the ^{224}Ra region by a weak random coincidence of ^{212}Bi line from the main decay branch. As all of the background events are expected to be random coincidences, the rate can be calculated as,

$$R_{\mathrm{Coin}} = \left(\frac{R_1 \cdot I_{\mathrm{Bi}}}{2}\right)^2 \cdot \Delta t \cdot \eta \quad (4)$$

where R_1 is the rate for a single alpha event from ^{224}Ra for a single detector and raised to the second power to account for random coincidences between the two detectors. The absolute intensity of ^{212}Bi is $I_{Bi} = 9.75(5)\,\%$ [35], and the timing resolution is given by Δt. The parameter η is the suppression factor accounting for the solid angle covered by the back-to-back pixels, the preliminary estimate obtained from the Monte Carlo simulation is described in the next section. For central pixels η is approximately 1.1×10^{-2}. Table 2 indicates that this random coincidence rate is for the present offline experiment exceptionally low, since the coincident rate is proportional to the square of the detected rate. This clearly shows that long measurement times, achievable only in offline experiments, are essential for high sensitivity in search of double-alpha decay in ^{224}Ra.

2.2. Monte-Carlo simulations of detector

Prior to the experiment, a preliminary model of the detector system was created using the GEANT4 simulation package [36] (version 10.2.0). The purpose of this model was to determine the effect of the geometry on the detection efficiency as well as to optimize geometric variables in the experiment, such as the distance between the detectors or the angle of the foil holder. The distance between the detectors was varied to see the effect on the solid angle and was set to 20 mm. The simulation assumed a dead layer of 0.8 µm silicon for the DSSDs. The sensitive area of the detectors was simulated to have a 49.5 mm to 49.5 mm area with a thickness of 1 mm silicon. The final position of each simulated event and the energy deposited in the detector were recorded. The used detector in this work has a strip width of 3 mm with a non-sensitive inter-strip pitch of 0.1 mm. After the simulation, this effect was mimicked by removing events that deposited their energy between the strips.

As already highlighted in Section 2.1, to successfully identify the predicted double-alpha decay events, the suppression of the background relative to single alpha events needs to exceed the predicted branching ratio of 10^{-8} for the back-to-back decay, resulting to at least an order of 10^{-9} suppression factor. This can be achieved by applying selection criteria in the analysis on the energy, space and time information of the events.

To carry out an efficient energy selection, both the double-alpha decay signal and the background from the decays of the child nuclei were simulated. To simulate the background, the full decay chain was simulated. The alpha particles in this simulation are emitted from the central source. As the main background is caused by random coincidence in the region of interest, the events of the two detectors were randomly mixed together to build the coincidence artificially. A simple region of interest was then constructed around the signal and the number of background events in that region was counted. The alphas detected at the edge of the DSSDs go through more of the dead layer than alphas detected at the center. The more dead layer the particle traverses, the worse the quality of the energy resolution as straggling becomes greater. A reduced energy resolution will lead to a reduced background suppression as the energy region must be enlarged to capture all signal events. The Monte Carlo simulation showed that the suppression by utilizing the energy information is 3.3×10^{-3} for central pixels and 1.3×10^{-2} for non-central pixels. In the final analysis, the energy selection will be further optimized to improve the signal-to-background ratio. The energy resolution was assumed to be 34 keV FWHM at $(\frac{1}{2}Q_{2\alpha})^{224Ra}$.

The random coincidences originating from alpha decay of the child nuclei can be suppressed by applying spatial selection criteria. Due to the symmetry of the detector system, the suppression factor is the sum of the opening angle of both (back-to-back decay) pixels divided by the total solid angle of the DSSDs. For the central pixels, this equals to 1.1×10^{-2} and increases for off-centered pixel pairs. However, this condition does come with an efficiency that is affected by the scattering of the alpha particle before detection and the geometry of the system. A study has been carried out to determine the magnitude of these effects. The scattering of an alpha particle was determined to decrease the back-to-back efficiency by 2.0 % assuming a foil thickness of 10 µg cm^{-2}. The effect of a beam spot determined by a simulation of the ion optics of 0.94 mm FWHM decreases efficiency of the back-to-back suppression by 14 % compared to a simulation of a point-like profile. The largest effect on the efficiency is a displacement between the two detectors on the plane defined by the axis of the beam and by the axis of the ladder. An offset of merely 2 mm reduces the efficiency of the suppression by 69 %. For this reason, the detectors were mounted on a holder which ensures the symmetry of the system. However, the exact position of implantation can be determined by analyzing the hit pattern on the detectors.

As mentioned, an important parameter for the back-to-back coincidence conditions is the size of the implantation beam spot. A study was performed comparing simulations with different sizes of beam spots. The measured hit pattern on the DSSDs was then used to determine if there was a sizable difference. It was found that the beam spot size could not be effectively determined from the hit pattern of the DSSD when below the pixel size.

Besides the energy and spatial selections, the time selection criterion is by far the most powerful condition to suppress background. The expected counting rate of approximately 1 kBq leads to a suppression of approximately 10^{-5} for a 20 ns time resolution.

The combination of the three selections should give a total suppression of approximately 10^{-9}, though every pixel will have a different value for the level that the background is suppressed.

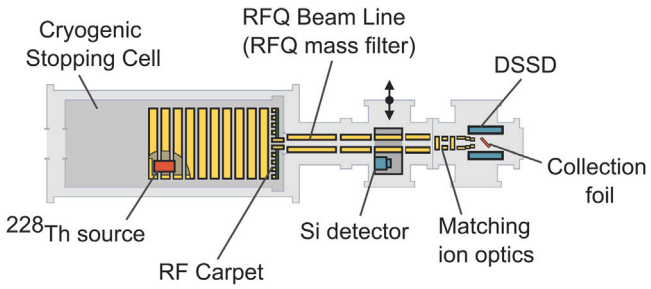

Fig. 1. Schematic overview of the FRS ion catcher with the experimental setup used to thermalize ^{224}Ra ions in the Cryogenic Stopping Cell (left), filter and transport them in the RFQ Beam Line (center) to the collection foil (right) for observation of decay in the DSSDs (right).

3. Experimental setup

A schematic overview of the FRS ion catcher with the new experimental setup is shown in Fig. 1. The system was composed of a CSC, a RFQ beam transport line that could be operated as a mass-filter, an ion-optical stage to focus the beam onto the collection foil, and the DSSD system. Each of these components is described in the following subsections.

3.1. Beam production, cryogenic stopping cell

Two thin, open commercial ^{228}Th sources with an initial total activity of 34.1(3) kBq (reference date 28th of January 2022, produced by the Eckert & Ziegler Group [37]) were mounted in the *INCREASE* version [38] of the CSC at GSI [22,39,40]. This configuration of the CSC has for a distance of 48.2 cm long ion thermalization region compared to ~100 cm long region in standard configuration developed to capture fast projectile fragments from the FRS separator. The CSC was filled with ultra-pure helium gas at 73 K and 30 mbar for a density of approximately 20 µg cm^{-3} corresponding to an areal density of approximately 1 mg cm^{-2}. The recoiling nuclei were thermalized in ultra-pure helium

gas and extracted from the cell as ions. Note that the kinetic energy of the recoiling ^{224}Ra ions is only 97.00(22) keV[19] for the strongest alpha decay branch, and thus the recoils have a range of less than 4 mm [41] in the cold helium buffer gas with the given density. The ^{228}Th alpha decay chain extends on from ^{224}Ra through ^{220}Rn, ^{216}Po, to ^{212}Pb and then branches through ^{212}Bi and ^{212}Po with beta and alpha decays ending in ^{208}Pb. Due to charge exchange with the He buffer gas and contaminants in the stopping cell, the ^{224}Ra ions were extracted mainly as doubly-charged ions due to the low second ionization potential, while ^{220}Rn, ^{216}Po, ^{212}Po and ^{212}Bi as singly charged ions. The ions were guided by a static electric field of approximately 8 V cm^{-1} away from the source towards an RF-carpet that draws the ions towards a central 0.7 mm diameter orifice. An important feature of the present system is the ability to select a given mass-to-charge ratio of the products using a system of radio-frequency quadrupole (RFQ) ion guides to produce a beam of ^{224}Ra^{2+}. The RF-carpet was operated in a mode to transport ions with an mass-to-charge ratio greater than approximately 100. This suppresses low mass (stable) ions [42]. Under these conditions, the mean extraction time from the CSC was estimated to be 70 ms.

3.2. RFQ beam line

The ions exiting the orifice were captured by an RFQ ion guide in a differentially pumped chamber maintained at $\sim 5 \times 10^{-3}$ mbar and room temperature. A small drag field transported the ions through the RFQ. A short section of the RFQ beam line was supported on a linear vertical drive that could move a silicon surface barrier (SSB) detector with a collection foil into the path of the beam (labeled "Si-detector" in Fig. 1). The SSB detector was used to monitor the number of short-lived alpha-emitting ions extracted from the CSC. Due to the long half-life of ^{224}Ra ions, the relatively short-lived isotope ^{220}Rn was used to tune the CSC and the beamline.

3.3. Matching and focusing ion optics

The final section of the beam delivery system was a differentially pumped section, consisting of an electrostatic beam transport (labeled as "ion optics"), including an einzel lens, a steerer, and a cone-shaped section between the two DSSDs to shield the beam from the DSSD bias, see Fig. 2. The cone was tapered to avoid shadowing the corner pixels on the DSSDs from the source and had a 3 mm diameter opening so as not to intercept the beam. The design of these ion optics were assisted by simulations using the SIMION code [43,44]. The simulations predict an implantation profile on the foil of less than 1 mm diameter (FHWM).

The ions were collected on a thin carbon foil placed at an angle of 55° with respect to the beam axis allowing the detection of back-to-back radiation in the central pixels of the DSSDs with the highest solid angles, see Fig. 3. The foil was held at negative 1 kV potential that provided the final acceleration of the ^{224}Ra^{2+} ions into the foil. The angle of the collection foil and its holder created a small asymmetry in the final electric field that caused the ions to deviate slightly from the center line of the setup; see Fig. 3 for an example of the final beam path calculated with the SIMION code [43,44]. The collection foil was made out of carbon with an areal density about 10 µg cm^{-2} (with a density of approximately 1.2 g cm^{-3}) that was located between the two DSSDs. Multiple foils with thicknesses of 9-13 µg cm^{-2} were mounted on frames in a ladder. This configuration allowed changes of the collector foil without opening up the vacuum chamber by moving the ladder vertically.

3.4. Detector setup

DSSDs are well suited as alpha detectors for this application. They produce signals that have typical rise times of the order of 10 ns or less [45]. These detectors will thus provide sufficient time resolution for good background suppression, given the total counting rate of the source. The orthogonal strips on the front and back of the silicon wafer define pixels. The spatial resolution simply depends on the size of the pixels, the distance to and size of the source. This provides reasonable positional resolution across the surface of the detector, but the solid angle subtended by each pixel will vary since the DSSD is flat while the source emits the particles in a spherical distribution.

Finally, careful attention to reducing electronic noise in the signal processing system can yield an energy resolution on the order of about 15 keV which allows clear differentiation of the predicted double-alpha energy from the individual decay energies. The optimal DSSDs do not need to be excessively thick since the range in silicon of the most energetic alpha particle in the decay chain is only 13.2 mg cm^{-2} or ~57 µm being 8.784 86(12) MeV from ^{212}Po [46]. Note, that the DSSDs have a dead layer that can be approximated as a 0.75 µm thick layer of aluminum on top of the silicon. Thus, alpha particles detected in a flat DSSD from a point source will have a systematic increase of the energy loss in the dead layer as one moves outward from the center pixels to the corner pixels due to the increased path length traveled by the alpha particles along the dead layer. Table 3 shows the calculated energy loss for the five most prominent alpha energies for normal incidence and also the average energy loss, ⟨ΔE⟩, at the central angle of the middle and corner pixels using the Standard Range Tables in the SRIM package [41].

The experiment used Micron Semiconductor Ltd (MSL) type W1 DSSDs [47]. Each detector has an active area of 49.5 × 49.5 mm^2, segmented into sixteen p^+n junction strips on the front and sixteen orthogonal n^+n ohmic strips on the back. The strip width is 3.0 mm and

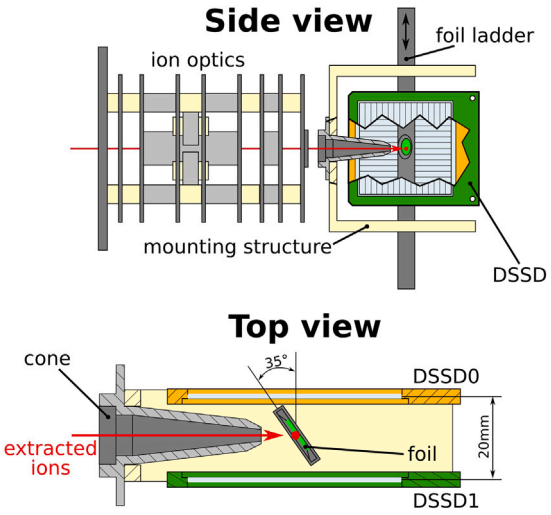

Fig. 2. Schematic illustration of the experimental setup with side and top views. The ions moved to the right onto the collection foil centered between the two DSSDs. Note that the ladder with the collection foil is tilted at 55° with respect to the beam axis. The actual positions of the detectors were slightly misaligned, see the text.

Table 3
Calculated values of the energy loss in MeV by the prominent alpha particles in the DSSD dead layer for normal incidence, and at the average angle for the central and corner pixels. See text for explanation.

Alpha Energy	ΔE Normal	⟨ΔE⟩ Central Px	⟨ΔE⟩ Corner Px
8.785	0.085	0.087	0.293
6.778	0.101	0.103	0.347
6.288	0.106	0.109	0.364
6.050	0.109	0.111	0.373
5.685	0.113	0.116	0.388

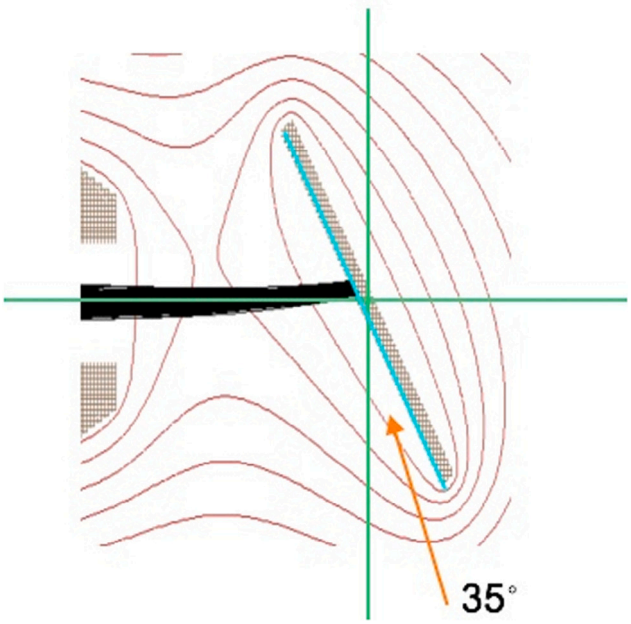

Fig. 3. Top view of the final path of the ions from the tip of the cone onto the foil calculated with the SIMION code. The ions (black lines) move from the left onto the collection foil centered between the two DSSDs. The red lines show equipotential contours. Note that the ions are bent as they approach the foil due to the slight asymmetry of the geometry.

the pitch size between the strips is 0.1 mm. The available thicknesses of the MSL type W1 DSSDs range from ∼ 50 µm, to 1500 µm [47]. For the present experiment, a pair of 1 mm thick DSSDs were used.

The present symmetric detector arrangement, with the detector faces parallel to one another, allowed a clear identification of potential back-to-back events based on the pixels in which events were observed. It was also desirable to minimize the separation between detectors and thus the distance to the implantation site and, thus, maximize the solid angles covered by the detectors. This option, however, contains a trade off since the solid angle of each pixel will vary strongly with position given the flat surfaces of the DSSDs. The central pixels of the DSSD will cover a much larger solid angle than the outer pixels. The choice of the optimum separation of the detectors also had to consider the total counting rate that will give an acceptable dead-time of the whole system.

With the ^{228}Th source strength and the established efficiencies for extraction and ion transport, an estimated counting rate of ∼ 1 kHz was used to balance the maximum counting rate per pixel with the solid-angle coverage of the two DSSDs. The separation between the two DSSDs was chosen to be about 2 cm. This distance provided a total solid angle coverage of 4.15 sr for each DSSD (33 % of 4π per detector), the central eight pixels (four on each detector) covering a solid angle of 0.4 sr.

The detectors were mounted on THORLABS [48] post holders which were secured to a THORLABS optical breadboard. The use of an optical breadboard allowed precise alignment and positioning of the detectors while allowing final adjustments of the detector positions or separation if required at a later date.

3.5. Data acquisition and electronics

The MSL type W1 DSSDs were instrumented using the RAL108 double-alpha preamplifiers and RAL109 shaping amplifier and discriminator modules developed by STFC Rutherford Appleton Laboratory and the University Edinburgh that have been used at a number of accelerator facilities [25,49,50].

The DSSDs were connected via two vacuum feedthroughs to two externally mounted 32-channel preamplifier modules. The preamplifier modules were directly mounted onto the vacuum flange to reduce the cable length from each DSSD to the preamplifier input in order to minimize the input capacitative load and extrinsic noise.

The RAL109 shaping amplifier outputs were connected to Silena 9418/6 V 32-channel, 12-bit VME ADCs, and the ECL outputs of the RAL109 discriminators were connected to external logic modules (to generate the DAQ trigger) and to a CAEN V767 128-channel VME TDC operating in the common-stop emulation mode [51]. The RAL109 discriminator thresholds were typically set to ∼500 keV to suppress signals from the energetic beta particles in the decay chain. The TDC and data acquisition trigger was the logical OR of all discriminator outputs.

Fixed amplitude pulser signals were sent to the test inputs of both RAL108 preamplifier modules to monitor the stability of the gain and offset of each channel. Positive and negative polarity signals were provided by an Ortec 448 Pulser [52] and Ortec 433 Sum & Invert Amplifier [52]. The pulser frequency was 50 Hz and continued to run throughout the experiment.

The VME ADCS, TDCs, and scaler were readout by a Motorola MVME 2434 CPU running the Multi-Instance Data Acquisition System (MIDAS) software [53] and the data were written to disk. Scaler data (e.g. triggers, triggers accepted, pulser events, etc.) were readout for every event and were used, for example, to monitor dead time and the readout of the fixed frequency pulser events also provided a 20 ms clock.

The data acquisition system was run at no more than 5 kHz in the present work so that the implantation rate was limited to be of the order of 1 kHz given that a fully equilibrated ^{224}Ra source emits a sequence of five alpha particles per decay.

4. Experiment

The double-alpha experiment was carried out in the vault of the final focus of the symmetric branch of the FRS at GSI and was independent of all other experiments taking place at the FRS. Therefore, to ensure undisturbed operation over a period of several month, a completely independent data acquisition system was installed, and a signal indicating that a beam pulse was extracted from the GSI synchrotron into the vault was included in the data stream. The commissioning and test phases using ions extracted from the CSC began in January 2022. The data-taking phase ran from February until the middle of July 2022, resulting in 123 days of measurement time. The achieved duration of a stable performance for the stopping cell was possible due to the development and implementation of a state-of-the-art slow control system [54]. The performance of the stopping cell deteriorated due to a leak towards the end of the experiment. As this was an offline experiment, it was possible to increase the run time by a factor of four to compensate for the lower rate. With the increased run time, the conditions described in Table 2 could still be met.

The experiment can be divided into three main phases according to the tuning of the mass filter. In the initial phase, lasting approximately 20 days, all of the extracted ions from the stopping cell were transported to the collection foil. In the main data-taking phase lasting approximately 80 days, mass filtering was applied to the extracted ion beam. Using the mass filter set to 105 u $< m/q <$ 180 u, about 35 % decrease in rate was observed for ^{220}Rn^{1+}, for ^{216}Po^{1+}, for ^{212}Po^{1+} and for ^{212}Bi^{1+} in comparison to the ^{224}Ra^{2+} rate measured by the DSSDs. Note that ^{212}Bi nuclei are one of the most critical sources of background, as they produce an alpha decay signal that is closest to the expected double-alpha energy from ^{224}Ra. However, it needs to be pointed out, that the maximum reduction of the implanted ^{212}Bi^{1+} rate is only a factor of two due to the continuous supply of ^{212}Bi from the ^{224}Ra decay. Various background measurements transporting only single charged ions were carried out during the final phase of data taking, which lasted about 20 days. In total, approximately 3×10^9 ^{224}Ra^{2+} ions were detected.

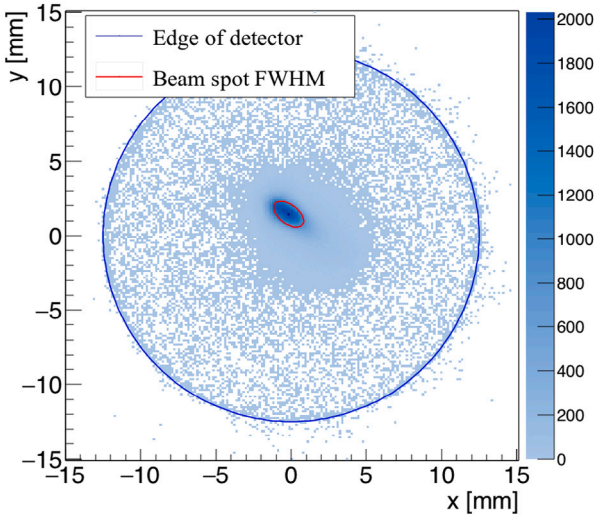

Fig. 4. A 2D histogram showing the hit pattern measured by the MCP system. The histogram is calibrated by using the edge of the MCP and setting the scale to the 25 mm active area. This is shown in the solid blue line. The solid red line shows the FWHM from a fit. Further details can be found in the text.

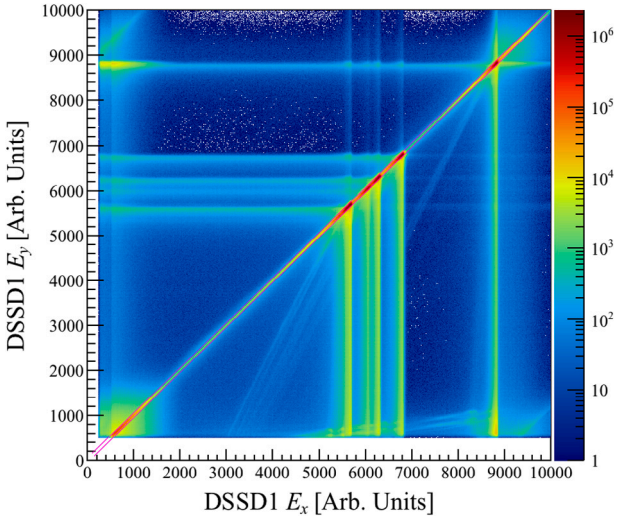

Fig. 5. The distribution of energy deposited on the front side of a detector (E_x) vs. the energy deposited in the back side of the detector (E_y) for the same event, for all events observed in DSSD1 is shown. Thin magenta lines indicate the position of the equal energy cut applied to the data.

5. Validation of beam spot size

As mentioned in Section 2.2, the two DSSDs are not sensitive to the size of the implantation spot if the implantation spot size is below the pixel size. However, the size of the implantation spot on the collection foil directly affects the efficiency of the back-to-back spatial selection condition. For this reason, an additional measurement has been carried out to determine the beam spot size.

The implantation spot was measured using a 3390 A 25 mm Open-Face microchannel plate (MCP) resistive anode encoder (RAE) detector system from Quantar Technology [55]. The anode surface of the RAE has a uniform resistance, meaning that the amplitude of the signal recorded at the four corners of the RAE is a linear function of the x and y positions. This signal is decoded by arithmetic processing and recorded for later analysis. For this detector setup, the spatial resolution is 250 μm FWFM.

The cone-shaped electrode and the DSSDs were removed at the end of the run to be able to host the MCP. The MCP was mounted onto the end of the ion optics to ensure that the beam spot had a 90° incident angle to the detector's surface. The voltages were kept at the same values as in the runs to keep experimental-like conditions. Measuring the beam spot profile in this way results in the real beam spot size and shape, as simulations show that the effect of the cone-shaped electrode on the beam spot is negligible.

The raw data from the RAE is calibrated by using the random events on the edge of the detector. The distribution is centered, and the scale is chosen so that the diameter of the active area is 25 mm. Then, the hit pattern is fitted with a Gaussian to find the beam spot and its characteristic dimensions, see Fig. 4. The FWHM of the beam spot is measured as 2.3(1) mm for x and 1.2(1) mm for y. This beam spot size is much smaller than the pixel size and thus sufficiently small to construct a rigorous back-to-back condition.

6. Single alpha particle events

This section presents important features of the spectra observed when individual alpha particles were detected in one of the DSSDs. The recorded energy distribution for an example dataset is shown in Fig. 5. The energy signals above the noise threshold from all strips on the junction side (so-called x-strips) are plotted against those from all of the strips on the ohmic side (so-called y-strips) for a single DSSD, for DSSD1. The horizontal and vertical straight lines apparent in the spectrum indicate interstrip effects for the x and y strips, respectively. In addition, all non-diagonal lines are a combination of this effect. In the case of an interstrip event, the collection of the generated charge carriers due to the energy deposited by the incident particle is shared between adjacent strips of the DSSD. The phenomena has been widely researched [56–62]. In order to filter out interstrip effects and thereby avoid its related energy reconstruction, a selection criterion was applied to the data that required nearly equal energy deposition in the x and y strips. The selection region ($\pm 3\sigma$) is shown within the parallel diagonal magenta lines in Fig. 5. Another phenomenon, that can be seen at the lower edge ($E_x, E_y < 2000$) of Fig. 5 as a diffuse pattern, is the effect of beta particles depositing their energy. An energetic beta particle scatters many times before depositing its full energy, and charge sharing between strips is more pronounced. Therefore, the introduced equal energy selection is an effective tool to suppress the beta background as well. While the equal energy condition helps to suppress the background of betas and of the interstrip effects, it does not change the detector efficiency significantly, as the majority of events fall within the magenta lines shown in Fig. 5. To reduce the background by β-decaying nuclides it is desirable to have a relatively thin detector to limit the amount of energy a β-particle deposits in the silicon while still allowing the full alpha particle energy to be collected, thus reducing pileup and the counting rate of the DAQ system given appropriate electronic thresholds. On the other hand, the energy and time resolution of a DSSD are inversely proportional to its capacitance, hence thicker detectors are often preferred. As the signal region of this measurement is dominated by alphas, the energy resolution was prioritized.

An energy calibration was performed on the data set, which was carried out in two stages. First, a relative gain and offset calibration was applied to the raw ADC data [63] from all 32 channels of each DSSD, which established a common arbitrary energy scale for all DSSD strips. Then the most prominent peaks in a single strip spectrum were assigned to the literature values of the expected alpha decay energies. The same calibration procedure was performed for both DSSDs. Following calibration, all of the prominent peaks in the spectrum could be clearly associated with a known alpha decay.

Fig. 6 shows the energy of single strip events measured on the junction side of DSSD1 for a central pixel. The alpha particles are essentially normally incident on this pixel. The alpha energy resolution

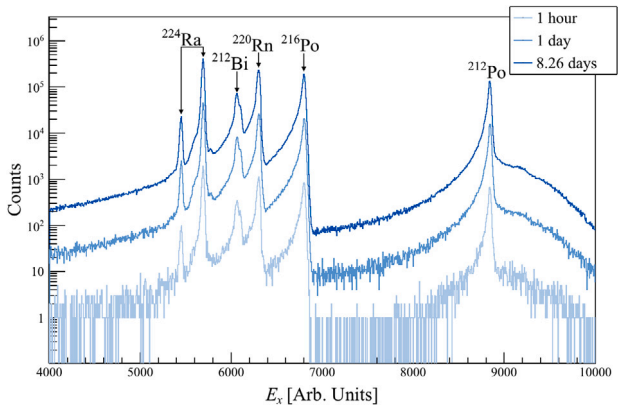

Fig. 6. Energy distribution from events in the x-side strips of a central pixel in DSSD1. The main peaks assigned to the alpha decays are labeled by the parent nucleus. The distribution is shown for 1 hour, 1 day, and 8.26 days of data taking. Good stability is observed in the gains.

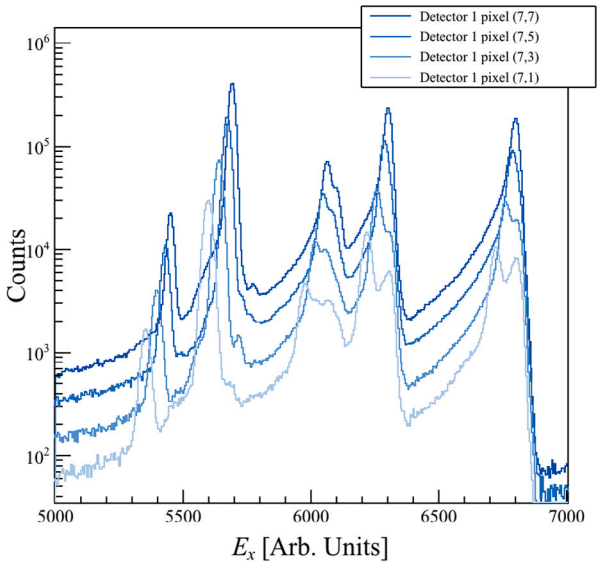

Fig. 7. Variation of the measured energy in various pixels that shows the effects of the dead layer and the incident angle. Note that the ^{224}Ra peaks, between 5600 and 5800 on this scale, move systematically to lower energies. In contrast, the other peaks from the child nuclei show this migration and some energy splitting, see text for details.

was found to be approximately 30 keV to 40 keV FWHM per strip with a significant low energy tail. The electronic noise measured with the pulser was of the order of 10 keV to 15 keV FWHM. Three examples, consecutive datasets with increasing measurement times are compared in this figure. The lowest, light blue, curve shows the dataset after 1 h of measurement, the middle, blue, curve was collected in one day of measurement, and the highest, dark blue, curve was collected in a little more than eight days of continuous measurement. Overall, good stability in the gain and offset was observed.

In Fig. 7 the measured energy spectra of four selected pixels on DSSD1 are shown. These pixels share a common x strip but moving away from the central region towards the edge of the DSSD, along the y axis. Two phenomena can be observed: the variation of the energy spectrum for central pixels as compared to edge pixels; and a splitting of all peaks other than the ^{224}Ra lines. These can be explained due to the effects of the dead layer of the detectors and due to the distribution of recoiling child nuclei onto the detector surfaces, respectively. All of the ^{224}Ra is expected to decay from the central implantation point, therefore, the alpha peaks corresponding to the decay of ^{224}Ra do not present splitting of the ^{224}Ra peak. However, the child nuclei following an initial decay of ^{224}Ra can reside either in the collection foil or on the front surface of a detector due to nuclear recoil and also radon effusion. In the latter case, the alpha particle from the decaying child nucleus is able to penetrate the dead layer nearly perpendicular on average to the dead layer, i.e., the smallest effective thickness, thus, with the lowest energy loss. In the former case of emission from the collection foil at the center, due to the incident angle of the alpha particle, the width of the effective dead layer and the related energy loss systematically increases. The energy difference between the two cases is in the order of few hundred keV (cf. Table 3) and causes the observed double peaking of the daughter decay lines seen in Fig. 7.

The so-called hit pattern or intensity map of each DSSD was constructed for the alpha decay events exclusively within the energy range of the ^{224}Ra decay energy for both peaks. Fig. 8 shows the data in an "open-book scheme" to provide an overall representation with an indication of the position of the foil holder relative to each detector. The left panel in this figure contains data from DSSD0 relative to the back side of the foil holder while the right panel contains data from DSSD1 relative to the front side of the foil holder. The ion beam moves from the left edge to the center on the left panel and from the right edge to the center on the right panel. The foil holder prevents the alpha particles emitted from the collection foil reaching the surface of the DSSDs due to its shadow. The so-called "shadow regions" can be recognized approximately 2 to 3 y-strips away from the foil holder. The location and the asymmetry of these regions are in good agreement with preliminary Monte Carlo simulations that take into account the overall geometry and the slightly off-center ion implantation on the foil. During the experiment the connection ceased to function between the x strip on the outermost edge of DSSD0 and the read out, which is indicated in Fig. 8 as an empty strip. The hit pattern shows the quality of the spatially resolved alpha data obtained during the run. In combination with the small beam spot size it should allow a suppression in accordance with the MonteCarlo estimate given in Section 2.2 by gating on a back to back alpha emission.

7. Coincident alpha particle events

This section contains a brief presentation of the important features of the coincident data and background suppression as discussed in Section 2.2. However, details of the full analysis will be presented in a subsequent manuscript. In addition to the predicted double-alpha decay from ^{224}Ra there is a decay predicted from ^{220}Rn as well. Even though the experiment is not optimized to be sensitive to this decay, it is still valuable to also search for the double-alpha decay of ^{220}Rn. However, the primary analysis focuses on the search for the ^{224}Ra double-alpha decay and is thus the main subject of this work.

The distribution of energy signals for DSSD0 in coincidence with DSSD1 with a time correlation window set only by the ADC trigger of approximately 2 μs is shown in Fig. 9 for all event multiplicities. The majority of events have a multiplicity of four (x and y strips on two detectors) but higher multiplicities are possible due to energy sharing between adjacent strips. The region relevant for possible double-alpha decay events was blinded; indicated by gray hashed bars. The figure is almost entirely dominated by random coincidences at the respective individual alpha energies. Additionally, an enhanced clustering of beta-alpha coincidences can be seen around the ^{212}Po alpha decay energy ($E_x \sim 8800$), which is a result of its short half-life of 294.3(8) ns[31] following the beta decay of ^{212}Bi. An interesting set of events can be seen in the lower left quadrant of the figure. These events follow ∼45° straight lines that can be assigned to Rutherford backscattering [64] of the daughter alpha particles. In this process, an alpha particle from the decay is elastically scattered under a generally large angle by the Coulomb field either of a Si nucleus in the detector medium or of an Al nucleus in the dead layer and then the scattered alpha particle reaches the other detector due to the close distance. This process is particularly

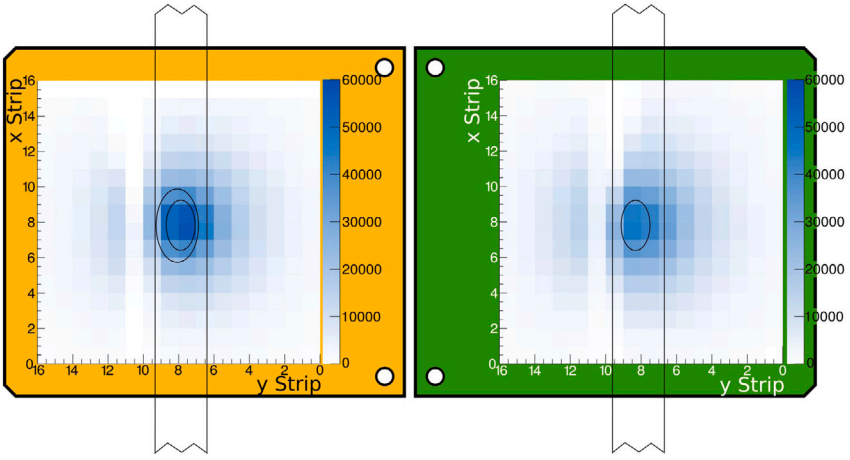

Fig. 8. The so-called hit pattern or intensity pattern of single events gated on the ^{224}Ra alpha decay energy in the two detectors. The illustration follows an "open-book scheme" for better visibility with an indication of the position of the foil holder. The left panel shows data from DSSD0, and the right panel from DSSD1. The patterns are generally symmetric as expected and clearly show the shadow from the foil holder. During the experiment, the connection was lost between the outermost $x = 15$ strip of DSSD0 and the read out. A detailed explanation of the figure is provided in the text.

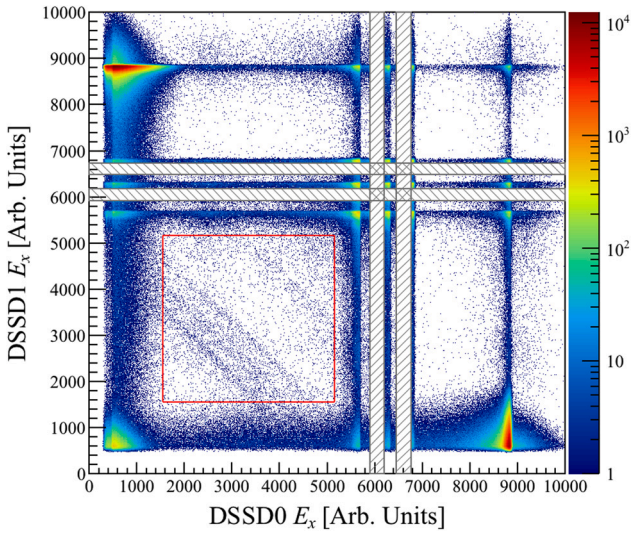

Fig. 9. Correlation plot of the observed energy signals in DSSD0 and DSSD1 with a large time correlation window set by the ADC gate width of approximately 2 μs. The red square indicates the region of "Rutherford" events, see text for further description. The gray hashed regions indicate the blind data with the expected double-alpha energy described in the text.

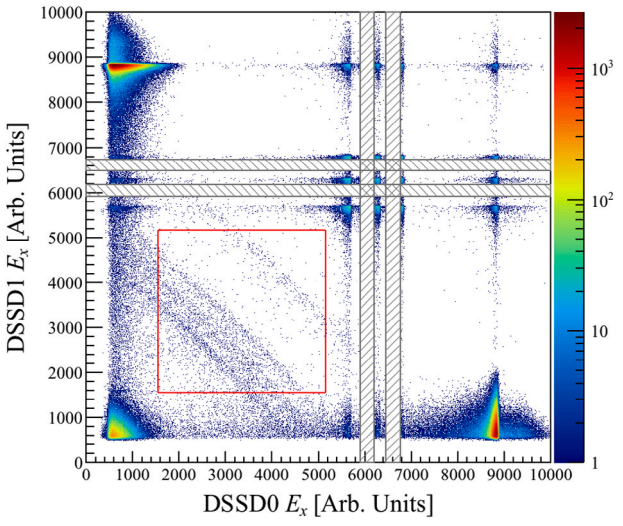

Fig. 10. Same as Fig. 9, but with a smaller correlation window set by the TDC to be 160 ns. Red box indicates the region of "Rutherford" events. Gray hashed regions blind the expected double-alpha energy regions, see text.

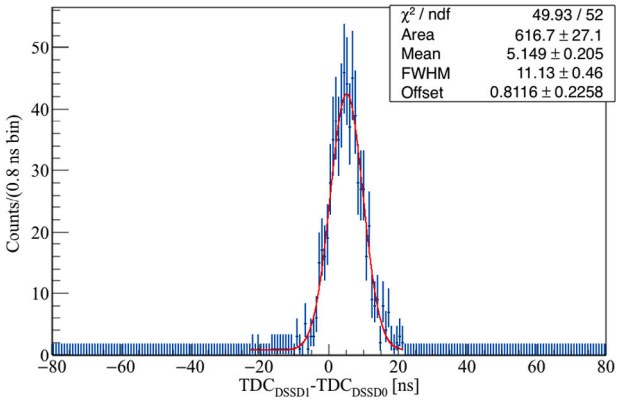

Fig. 11. Uncorrected TDC time difference between DSSD0 and DSSD1 gated on Rutherford events (Events within a box between 2 MeV to 3 MeV). Note that this region is almost entirely free from random coincidences.

enhanced in the present case when the recoil nuclei are deposited on the front surface of one DSSD. The sharing of the total alpha decay energy occurs between the initial emission with nuclear recoil in one detector and the signal from the scattered alpha particle in the other detector. The scattering phenomena become more apparent when a more stringent time gate is set on the data. Fig. 10 shows events with a 160 ns coincidence gate that was set in the TDC data. The more stringent gate dramatically reduced the number of random coincidences but left the number of Rutherford backscattering events essentially unchanged. In fact, the Rutherford backscattering events provided a convenient measurement of the coincidence timing resolution of the two DSSD. Even without correcting for energy-dependent timing effects such as amplitude walk of the RAL109 leading edge discriminator, the time difference between DSSD0 and DSSD1 gated on "Rutherford" events with energy signals between 2 MeV to 3 MeV is approximately 11 ns FWHM as shown in Fig. 11 and gives an upper limit for the expected time resolution of the overall system.

A detailed blinded analysis is currently ongoing and will explore the ultimate performance characteristics of the setup further as well as address the search for simultaneous double-alpha decay. In order not to bias any future analysis, the alpha energy region in each DSSD defined as $\frac{1}{2}Q_{2\alpha} \pm 4\sigma_{Ex}$ was removed from the analysis for each of the two candidate nuclei. Also, the lower energy bound was reduced by an additional ~90 keV to take into account energy loss in the dead layer.

8. Summary and outlook

In summary, the FRS Ion Catcher has been extended with a new experimental apparatus, which allows using a strong, purified source of isotopes produced from alpha decay for high-statistics studies of their decay, in particular for the search for exotic decay modes in these nuclides by implanting them in a thin carbon foil held between two large area double-sided silicon-strip detectors. To optimize the size of the implantation spot on the foil to the sub-millimeter level, an electrostatic matching ion optics was built and the implantation profile was measured with a position-sensitive MCP detector. In the experiment reported here, a ^{228}Th source was used in the cryogenic stopping cell of the FRS Ion Catcher to produce $^{224}Ra^{2+}$ ion, which have been identified as a strong candidate for the observation of a new nuclear decay mode in which two alpha particles are simultaneously emitted in opposite directions from the decaying nucleus. The radium nuclei are the first decay products of a long chain of alpha emitters that end with ^{208}Pb. An important feature in this experiment is the ability to suppress the child activity by separating the 2^+ radium ions from the 1^+ children operating the RFQ beamline mass-selectively as an RFQ mass filter. In the experiment, we were able to measure the correlated decay events in terms of position, energy, and time over a period of approximately 123 days and observed the decay of approximately 3×10^9 radium nuclei. The data from the search for the new decay mode is under analysis, and the results will be described in a future publication.

As mentioned in Section 2.1, a higher source strength alone will not increase the sensitivity to this rare decay. A possible improvement could be to enhance the timing resolution, which would open the possibility of using a larger source strength. Detectors with smaller pixelization would also give the ability to constrain random back-to-back coincidences. The combination of these improvements should increase the sensitivity by an order of magnitude.

Currently, it is not resolved how the background from ^{212}Bi can be further suppressed in a future experiment using ^{224}Ra. It is possible to try to find other isotopes that do not have this background, but most of the candidates are short living. Then, a dedicated setup can be built based on the technique shown in this work for which the run time could be significantly extended.

CRediT authorship contribution statement

L. Varga: Writing – review & editing, Writing – original draft, Methodology, Investigation, Formal analysis, Data curation. **H. Wilsenach:** Writing – review & editing, Writing – original draft, Software, Methodology, Investigation, Formal analysis, Data curation. **O. Hall:** Software, Methodology, Investigation, Data curation. **T. Dickel:** Writing – review & editing, Writing – original draft, Supervision, Project administration, Methodology, Investigation, Funding acquisition, Conceptualization. **M.P. Reiter:** Writing – review & editing, Writing – original draft, Supervision, Methodology, Investigation, Funding acquisition, Data curation, Conceptualization. **D. Amanbayev:** Methodology. **T. Davinson:** Writing – review & editing, Writing – original draft, Methodology, Investigation, Formal analysis, Data curation. **D.J. Morrissey:** Writing – review & editing, Writing – original draft, Supervision, Methodology, Investigation, Formal analysis, Data curation, Conceptualization. **I. Pohjalainen:** Methodology. **N. Tortorelli:** Methodology. **J. Yu:** Methodology. **J. Zhao:** Methodology. **S. Ayet:** Methodology. **S. Beck:** Methodology. **J. Bergmann:** Methodology. **Z. Ge:** Methodology. **H. Geissel:** Methodology. **L. Heitz:** Methodology. **C. Hornung:** Methodology. **N. Kalantar-Nayestanaki:** Methodology. **E. Khan:** Writing – review & editing, Writing – original draft, Methodology, Investigation, Formal analysis, Conceptualization. **G. Kripko-Koncz:** Methodology. **I. Mardor:** Methodology. **M. Narang:** Methodology. **W. Plass:** Methodology. **C. Scheidenberger:** Supervision, Methodology, Investigation, Conceptualization. **M. Simonov:** Methodology. **S.K. Singh:** Methodology. **A. State:** Methodology. **M. Vandebrouck:** Methodology. **P.J. Woods:** Supervision, Methodology, Investigation, Conceptualization. **FRS Ion Catcher Collaboration:** Supervision, Resources, Project administration, Methodology, Investigation, Conceptualization.

Declaration of competing interest

The authors declare that they have no known competing financial interests or personal relationships that could have appeared to influence the work reported in this paper.

Data availability

Data will be made available on request.

Acknowledgments

In memory of Christophe Theisen, whose unparalleled dedication, insightful contributions, and unwavering commitment were pivotal in shaping of this research.

We would like to thank Dr. Bettina Lommel and Dr. Birgit Kindler from the GSI Target Laboratory for preparing the carbon foils used in this experiment.

This work was supported by UK Science and Technology Facilities Council STFC Grant No: ST/P004008/1 and ST/V001051/1, by the German Federal Ministry for Education and Research (BMBF) under contracts no. 05P19RGFN1 and 05P21RGFN1, by HGS-HIRe, and by Justus-Liebig-Universität Gießen and GSI under the JLU-GSI strategic Helmholtzpartnership agreement. This research was supported in part by the ExtreMe Matter Institute EMMI at the GSI Helmholtzzentrum für Schwerionenforschung, Darmstadt.

The work leading to this publication was supported by the PRIME programme of the German Academic Exchange Service (DAAD) with funds from the German Federal Ministry of Education and Research (BMBF). The project was also supported by the dean of exact science's fellowship from Tel Aviv University. This work was carried out under the contract PN 23.21.01.06 sponsored by the Romanian Ministry of Research, Innovation and Digitalization.

The work leading to this publication was supported by the Deutsche Forschungsgemeinschaft (DFG, German Research Foundation) - AY 155/2-1.

References

[1] C. Walz, H. Scheit, N. Pietralla, et al., Observation of the competitive double-gamma nuclear decay, Nature 526 (2015) 406–409, http://dx.doi.org/10.1038/nature15543.

[2] D.E. Alburger, P.D. Parker, Search for double Gamma-ray emission from the first excited states of O^{16} and C^{12}, Phys. Rev. 135 (1964) B294–B300, http://dx.doi.org/10.1103/PhysRev.135.B294.

[3] M. Goeppert-Mayer, Double beta-disintegration, Phys. Rev. 48 (1935) 512–516, http://dx.doi.org/10.1103/PhysRev.48.512.

[4] A.S. Barabash, Experiment double beta decay: Historical review of 75 years of research, Phys. At. Nucl. 74 (4) (2011) 603–613, http://dx.doi.org/10.1134/S1063778811030070.

[5] M. Agostini, M. Allardt, A.M. Bakalyarov, M. Balata, I. Barabanov, N. Barros, L. Baudis, C. Bauer, N. Becerici-Schmidt, E. Bellotti, S. Belogurov, S.T. Belyaev, G. Benato, A. Bettini, L. Bezrukov, T. Bode, D. Borowicz, V. Brudanin, R. Brugnera, D. Budjáš, A. Caldwell, C. Cattadori, A. Chernogorov, V. D'Andrea, E.V. Demidova, A. di Vacri, A. Domula, E. Doroshkevich, V. Egorov, R. Falkenstein, O. Fedorova, K. Freund, N. Frodyma, A. Gangapshev, A. Garfagnini, P. Grabmayr, V. Gurentsov, K. Gusev, A. Hegai, M. Heisel, S. Hemmer, G. Heusser, W. Hofmann, M. Hult, L.V. Inzhechik, J.J. Csáthy, J. Jochum, M. Junker, V. Kazalov, T. Kihm, I.V. Kirpichnikov, A. Kirsch, A. Klimenko, K.T. Knöpfle, O. Kochetov, V.N. Kornoukhov, V.V. Kuzminov, M. Laubenstein, A. Lazzaro, V.I. Lebedev, B. Lehnert, H.Y. Liao, M. Lindner, I. Lippi, A. Lubashevskiy, B. Lubsandorzhiev, G. Lutter, C. Macolino, B. Majorovits, W. Maneschg, E. Medinaceli, M. Misiaszek, P. Moseev, I. Nemchenok, D. Palioselitis, K. Panas, L. Pandola, K. Pelczar, A. Pullia, S. Riboldi, N. Rumyantseva, C. Sada, M. Salathe, C. Schmitt, B. Schneider, S. Schönert, J. Schreiner, A.-K. Schütz, O. Schulz, B. Schwingenheuer, O. Selivanenko, M. Shirchenko, H. Simgen, A. Smolnikov, L. Stanco, M. Stepaniuk, C.A. Ur, L. Vanhoefer, A.A. Vasenko, A. Veresnikova, K. von Sturm, V. Wagner, M. Walter, A. Wegmann, T. Wester, H. Wilsenach, M. Wojcik, E. Yanovich, P. Zavarise, I. Zhitnikov, S.V. Zhukov, D. Zinatulina, K. Zuber, G. Zuzel, Results on $\beta\beta$ decay with emission of two neutrinos or Majorons in ^{76}Ge from GERDA Phase I, Eur. Phys. J. C 75 (9) (2015) http://dx.doi.org/10.1140/epjc/s10052-015-3627-y.

[6] M. Pfützner, E. Badura, C. Bingham, B. Blank, M. Chartier, H. Geissel, J. Giovinazzo, L.V. Grigorenko, R. Grzywacz, M. Hellström, Z. Janas, J. Kurcewicz, A.S. Lalleman, C. Mazzocchi, I. Mukha, G. Münzenberg, C. Plettner, E. Roeckl, K.P. Rykaczewski, K. Schmidt, R.S. Simon, M. Stanoiu, J.-C. Thomas, First evidence for the two-proton decay of ^{45}Fe, Eur. Phys. J. A - Hadrons Nucl. 14 (3) (2002) 279–285.

[7] J. Giovinazzo, B. Blank, M. Chartier, S. Czajkowski, A. Fleury, M.J. Lopez Jimenez, M.S. Pravikoff, J.-C. Thomas, F. de Oliveira Santos, M. Lewitowicz, V. Maslov, M. Stanoiu, R. Grzywacz, M. Pfützner, C. Borcea, B.A. Brown, Two-proton radioactivity of ^{45}Fe, Phys. Rev. Lett. 89 (2002) 102501, http://dx.doi.org/10.1103/PhysRevLett.89.102501, URL https://link.aps.org/doi/10.1103/PhysRevLett.89.102501.

[8] A. Spyrou, Z. Kohley, T. Baumann, D. Bazin, B.A. Brown, G. Christian, P.A. DeYoung, J.E. Finck, N. Frank, E. Lunderberg, S. Mosby, W.A. Peters, A. Schiller, J.K. Smith, J. Snyder, M.J. Strongman, M. Thoennessen, A. Volya, First observation of ground state dineutron decay: ^{16}Be, Phys. Rev. Lett. 108 (2012) 102501, http://dx.doi.org/10.1103/PhysRevLett.108.102501.

[9] D. Poenaru, M. Ivascu, Two alpha, three alpha and multiple heavy-ion radioactivities, J. Physique Lett. 46 (13) (1985) 591–594, http://dx.doi.org/10.1051/jphyslet:019850046013059100, URL http://www.edpsciences.org/10.1051/jphyslet:019850046013059100.

[10] P. De Marcillac, N. Coron, G. Dambier, J. Leblanc, J.-P. Moalic, Experimental detection of α-particles from the radioactive decay of natural bismuth, Nature 422 (6934) (2003) 876–878.

[11] V. Tretyak, Spontaneous double alpha decay: First experimental limit and prospects of investigation, Nucl. Phys. At. Energy 22 (2) (2021) 121–126, http://dx.doi.org/10.15407/jnpae2021.02.121, URL http://jnpae.kinr.kiev.ua/22.2/html/22.2.0121.html.

[12] K.P. Santhosh, T.A. Jose, Theoretical investigation on double-α decay from radioactive nuclei, Phys. Rev. C 104 (2021) 064604, http://dx.doi.org/10.1103/PhysRevC.104.064604, URL https://link.aps.org/doi/10.1103/PhysRevC.104.064604.

[13] M. Chandran, K.P. Santhosh, α and 2α decay of nuclei in the region $94 \leq Z \leq 101$ using the modified generalized liquid drop model, Phys. Rev. C 107 (2023) 024614, http://dx.doi.org/10.1103/PhysRevC.107.024614, URL https://link.aps.org/doi/10.1103/PhysRevC.107.024614.

[14] F. Mercier, J. Zhao, J.P. Ebran, E. Khan, T. Nikšić, D. Vretenar, Microscopic description of 2α decay in ^{212}Po and ^{224}Ra isotopes, Phys. Rev. Lett. 127 (1) (2021) 1–6, http://dx.doi.org/10.1103/PhysRevLett.127.012501.

[15] V. Denisov, Estimation of the double alpha-decay half-life, Phys. Lett. B 835 (2022) 137569, http://dx.doi.org/10.1016/j.physletb.2022.137569, URL https://www.sciencedirect.com/science/article/pii/S0370269322007031.

[16] J. Zhao, J.-P. Ebran, L. Heitz, E. Khan, F. Mercier, T. Nikšić, D. Vretenar, Microscopic description of $\alpha, 2\alpha$, and cluster decays of $^{216-220}$Rn and $^{220-224}$Ra, Phys. Rev. C 107 (2023) 034311, http://dx.doi.org/10.1103/PhysRevC.107.034311, URL https://link.aps.org/doi/10.1103/PhysRevC.107.034311.

[17] H.J. Rose, G.A. Jones, A new kind of natural radioactivity, Nature 307 (5948) (1984) 245–247, http://dx.doi.org/10.1038/307245a0.

[18] D.N. Poenaru, Y. Nagame, R.A. Gherghescu, W. Greiner, Systematics of cluster decay modes, Phys. Rev. C 65 (2002) 054308, http://dx.doi.org/10.1103/PhysRevC.65.054308, URL https://link.aps.org/doi/10.1103/PhysRevC.65.054308.

[19] K. Abusaleem, Nuclear data sheets for A=228, Nucl. Data Sheets 116 (2014) 163–262, http://dx.doi.org/10.1016/j.nds.2014.01.002, URL https://www.sciencedirect.com/science/article/pii/S0090375214000118.

[20] P.B. Price, J.D. Stevenson, S.W. Barwick, H.L. Ravn, Discovery of radioactive decay of ^{222}Ra and ^{224}Ra by ^{14}C emission, Phys. Rev. Lett. 54 (1985) 297–299, http://dx.doi.org/10.1103/PhysRevLett.54.297, URL https://link.aps.org/doi/10.1103/PhysRevLett.54.297.

[21] W. Plaß, T. Dickel, S. Purushothaman, P. Dendooven, H. Geissel, J. Ebert, E. Haettner, C. Jesch, M. Ranjan, M. Reiter, H. Weick, F. Amjad, S. Ayet, M. Diwisch, A. Estrade, F. Farinon, F. Greiner, N. Kalantar-Nayestanaki, R. Knöbel, J. Kurcewicz, J. Lang, I. Moore, I. Mukha, C. Nociforo, M. Petrick, M. Pfützner, S. Pietri, A. Prochazka, A.-K. Rink, S. Rinta-Antila, D. Schäfer, C. Scheidenberger, M. Takechi, Y. Tanaka, J. Winfield, M. Yavor, The FRS Ion Catcher – A facility for high-precision experiments with stopped projectile and fission fragments, Nucl. Instrum. Methods Phys. Res. B 317 (PART B) (2013) 457–462, http://dx.doi.org/10.1016/j.nimb.2013.07.063, URL https://linkinghub.elsevier.com/retrieve/pii/S0168583X13008823.

[22] S. Purushothaman, M. Reiter, E. Haettner, P. Dendooven, T. Dickel, H. Geissel, J. Ebert, C. Jesch, W. Plaß, M. Ranjan, H. Weick, F. Amjad, S. Ayet, M. Diwisch, A. Estrade, F. Farinon, F. Greiner, N. Kalantar-Nayestanaki, R. Knöbel, J. Kurcewicz, J. Lang, I. Moore, I. Mukha, C. Nociforo, M. Petrick, M. Pfuetzner, S. Pietri, A. Prochazka, A.-K. Rink, S. Rinta-Antila, C. Scheidenberger, M. Takechi, Y. Tanaka, J. Winfield, M. Yavor, First online results of a cryogenic stopping cell with short-lived heavy uranium fragments produced at 1000 MeV/u, Eur. Phys. Lett. 104 (2013) 42001, http://dx.doi.org/10.1209/0295-5075/104/42001.

[23] W. Zhang, B. Cederwall, Ö. Aktas, X. Liu, A. Ertoprak, A. Nyberg, K. Auranen, B. Alayed, H. Badran, H. Boston, M. Doncel, U. Forsberg, T. Grahn, P.T. Greenlees, S. Guo, J. Heery, J. Hilton, D. Jenkins, R. Julin, S. Juutinen, M. Luoma, O. Neuvonen, J. Ojala, R.D. Page, J. Pakarinen, J. Partanen, E.S. Paul, C. Petrache, P. Rahkila, P. Ruotsalainen, M. Sandzelius, J. Sarén, S. Szwec, H. Tann, J. Uusitalo, R. Wadsworth, Observation of the proton emitter $^{116}_{57}$La$_{59}$, Commun. Phys. 5 (1) (2022) http://dx.doi.org/10.1038/s42005-022-01069-w.

[24] Handbook of Nuclear Physics, Springer Nature Singapore, 2020, http://dx.doi.org/10.1007/978-981-15-8818-1.

[25] P. Sellin, P. Woods, D. Branford, T. Davinson, N. Davis, D. Ireland, K. Livingston, R. Page, A. Shotter, S. Hofmann, R. Hunt, A. James, M. Hotchkis, M. Freer, S. Thomas, A double-sided silicon strip detector system for proton radioactivity studies, Nucl. Instrum. Methods Phys. Res. A 311 (1–2) (1992) 217–223, http://dx.doi.org/10.1016/0168-9002(92)90867-4, URL https://www.sciencedirect.com/science/article/pii/0168900292908674.

[26] C.N. Davids, Experimental and theoretical aspects of proton radioactivity: Proton decay of spherical and deformed nuclei, in: D.N. Poenaru, H. Rebel, J. Wentz (Eds.), Nuclei Far from Stability and Astrophysics, Springer Netherlands, Dordrecht, 2001, pp. 79–89, http://dx.doi.org/10.1007/978-94-010-0708-5_7.

[27] D.T.J. R. D. Page, Proton emission—Recent results and future prospects, Nucl. Phys. Rev. 2 (33) (2016) 180–183, http://dx.doi.org/10.11804/NuclPhysRev.33.02.180.

[28] Z. Meisel, M. del Santo, H. Crawford, R. Cyburt, G. Grinyer, C. Langer, F. Montes, H. Schatz, K. Smith, β -Particle energy-summing correction for β -delayed proton emission measurements, Nucl. Instrum. Methods Phys. Res. A 844 (2017) 45–52, http://dx.doi.org/10.1016/j.nima.2016.11.019.

[29] M.V. Lund, A. Andreyev, M.J.G. Borge, J. Cederkäll, H. De Witte, L.M. Fraile, H.O.U. Fynbo, P.T. Greenlees, L.J. Harkness-Brennan, A.M. Howard, M. Huyse, B. Jonson, D.S. Judson, O.S. Kirsebom, J. Konki, J. Kurcewicz, I. Lazarus, R. Lica, S. Lindberg, M. Madurga, N. Marginean, R. Marginean, I. Marroquin, C. Mihai, M. Munch, E. Nacher, A. Negret, T. Nilsson, R.D. Page, S. Pascu, A. Perea, V. Pucknell, P. Rahkila, E. Rapisarda, K. Riisager, F. Rotaru, C. Sotty, M. Stanoiu, O. Tengblad, A. Turturica, P. Van Duppen, V. Vedia, R. Wadsworth, N. Warr, I.D.S. Collaboration, Beta-delayed proton emission from 20Mg, Eur. Phys. J. A 52 (10) (2016) 304, http://dx.doi.org/10.1140/epja/i2016-16304-x.

[30] R. McPherson, J. Hardy, R. Bell, Delayed proton emission following the decay of Ne17, Phys. Lett. 11 (1) (1964) 65–67, http://dx.doi.org/10.1016/0031-9163(64)90261-6, URL https://www.sciencedirect.com/science/article/pii/0031916364902616.

[31] E. Browne, J. Tuli, Nuclear data sheets for A=220, Nucl. Data Sheets 112 (4) (2011) 1115–1161, http://dx.doi.org/10.1016/j.nds.2011.03.002, URL https://www.sciencedirect.com/science/article/pii/S0090375211000214.

[32] S.-C. Wu, Nuclear data sheets for A=216, Nucl. Data Sheets 108 (5) (2007) 1057–1092, http://dx.doi.org/10.1016/j.nds.2007.04.001, URL https://www.sciencedirect.com/science/article/pii/S0090375207000415.

[33] K. Auranen, E. McCutchan, Nuclear data sheets for A=212, Nucl. Data Sheets 168 (2020) 117–267, http://dx.doi.org/10.1016/j.nds.2020.09.002, URL https://www.sciencedirect.com/science/article/pii/S0090375220300351.

[34] M. Martin, Nuclear data sheets for A=208, Nucl. Data Sheets 108 (8) (2007) 1583–1806, http://dx.doi.org/10.1016/j.nds.2007.07.001, URL https://www.sciencedirect.com/science/article/pii/S0090375207000658.

[35] M. Martin, Nuclear data sheets for A=208, Nucl. Data Sheets 108 (8) (2007) 1583–1806, http://dx.doi.org/10.1016/j.nds.2007.07.001.

[36] J. Allison, K. Amako, J. Apostolakis, P. Arce, M. Asai, T. Aso, E. Bagli, A. Bagulya, S. Banerjee, G. Barrand, B. Beck, A. Bogdanov, D. Brandt, J. Brown, H. Burkhardt, P. Canal, D. Cano-Ott, S. Chauvie, K. Cho, G. Cirrone, G. Cooperman, M. Cortés-Giraldo, G. Cosmo, G. Cuttone, G. Depaola, L. Desorgher, X. Dong, A. Dotti, V. Elvira, G. Folger, Z. Francis, A. Galoyan, L. Garnier, M. Gayer, K. Genser, V. Grichine, S. Guatelli, P. Guèye, P. Gumplinger, A. Howard, I. Hřivnáčová, S. Hwang, S. Incerti, A. Ivanchenko, V. Ivanchenko, F. Jones, S. Jun, P. Kaitaniemi, N. Karakatsanis, M. Karamitros, M. Kelsey, A. Kimura, T. Koi, H. Kurashige, A. Lechner, S. Lee, F. Longo, M. Maire, D. Mancusi, A. Mantero,

E. Mendoza, B. Morgan, K. Murakami, T. Nikitina, L. Pandola, P. Paprocki, J. Perl, I. Petrović, M. Pia, W. Pokorski, J. Quesada, M. Raine, M. Reis, A. Ribon, A. Ristić Fira, F. Romano, G. Russo, G. Santin, T. Sasaki, D. Sawkey, J. Shin, I. Strakovsky, A. Taborda, S. Tanaka, B. Tomé, T. Toshito, H. Tran, P. Truscott, L. Urban, V. Uzhinsky, J. Verbeke, M. Verderi, B. Wendt, H. Wenzel, D. Wright, D. Wright, T. Yamashita, J. Yarba, H. Yoshida, Recent developments in Geant4, Nucl. Instrum. Methods Phys. Res. A 835 (2016) 186–225, http://dx.doi.org/10.1016/j.nima.2016.06.125, URL https://www.sciencedirect.com/science/article/pii/S0168900216306957.

[37] Eckert & Ziegler Group, https://www.ezag.com/home/. (Online; accessed 14 June 2023).

[38] A. Rotaru, D. Amanbayev, D. Balabanski, D. Benyamin, P. Constantin, T. Dickel, L. Gröf, I. Mardor, I. Miskun, D. Nichita, W. Plaß, C. Scheidenberger, A. Spătaru, A. State, INCREASE: An in-cell reaction system for multi-nucleon transfer and spontaneous fission at the FRS Ion Catcher, Nucl. Instrum. Methods Phys. Res. B 512 (2022) 83–90, http://dx.doi.org/10.1016/j.nimb.2021.11.018.

[39] M. Ranjan, S. Purushothaman, T. Dickel, H. Geissel, W.R. Plass, D. Schäfer, C. Scheidenberger, J.V. de Walle, H. Weick, P. Dendooven, New stopping cell capabilities: RF carpet performance at high gas density and cryogenic operation, Europhys. Lett. 96 (5) (2011) 52001, http://dx.doi.org/10.1209/0295-5075/96/52001.

[40] M. Ranjan, P. Dendooven, S. Purushothaman, T. Dickel, M. Reiter, S. Ayet, E. Haettner, I. Moore, N. Kalantar-Nayestanaki, H. Geissel, W. Plaß, D. Schäfer, C. Scheidenberger, F. Schreuder, H. Timersma, J. Van de Walle, H. Weick, Design, construction and cooling system performance of a prototype cryogenic stopping cell for the Super-FRS at FAIR, Nucl. Instrum. Methods Phys. Res. A 770 (2015) 87–97, http://dx.doi.org/10.1016/j.nima.2014.09.075, URL https://www.sciencedirect.com/science/article/pii/S0168900214011073.

[41] J.F. Ziegler, M.D. Ziegler, J.P. Biersack, SRIM - The stopping and range of ions in matter (2010), Nucl. Instrum. Methods Phys. Res. B 268 (11–12) (2010) 1818–1823, http://dx.doi.org/10.1016/j.nimb.2010.02.091.

[42] I. Miskun, T. Dickel, S.A. San Andrés, J. Bergmann, P. Constantin, J. Ebert, H. Geissel, F. Greiner, E. Haettner, C. Hornung, W. Lippert, I. Mardor, I. Moore, W.R. Plaß, S. Purushothaman, A.-K. Rink, M.P. Reiter, C. Scheidenberger, H. Weick, Separation of atomic and molecular ions by ion mobility with an RF carpet, Int. J. Mass Spectrom. 459 (2021) 116450, http://dx.doi.org/10.1016/j.ijms.2020.116450, URL https://www.sciencedirect.com/science/article/pii/S1387380620303730.

[43] D. Dahl, SIMION for the personal computer in reflection, Int. J. Mass Spectrom. 200 (2000).

[44] Scientific Instrument Services, SIMION, 2023, http://www.simion.com/.

[45] A.A. Quaranta, M. Martini, G. Ottaviani, The pulse shape and the timing problem in solid state detectors - A review paper, IEEE Trans. Nucl. Sci. 16 (2) (1969) 35–61, http://dx.doi.org/10.1109/TNS.1969.4325151, URL http://ieeexplore.ieee.org/document/4325151/.

[46] National Institute for Science and Technology; Stopping Power and Range Tables for Alpha Particles, https://physics.nist.gov/PhysRefData/Star/Text/ASTAR.html. (Online; accessed 18 November 2022).

[47] Micron Semiconductor Ltd., http://www.micronsemiconductor.co.uk/. (Online; accessed 01 August 2023).

[48] Thorlabs, Inc., https://www.thorlabs.com/. (Online; accessed 04 June 2023).

[49] T. Davinson, A. Shotter, E. Macdonald, et al., Development of a silicon strip detector array for nuclear structure physics, Nucl. Instrum. Methods Phys. Res. A 288 (1) (1990) 245–249, http://dx.doi.org/10.1016/0168-9002(90)90493-P, URL https://www.sciencedirect.com/science/article/pii/016890029090493P.

[50] S. Thomas, T. Davinson, A. Shotter, A modular amplifier system for the readout of silicon strip detectors, Nucl. Instrum. Methods Phys. Res. A 288 (1) (1990) 212–218, http://dx.doi.org/10.1016/0168-9002(90)90488-R, URL https://www.sciencedirect.com/science/article/pii/016890029090488R.

[51] CA.E.N V767 128 Channel Multihit TDC, https://www.caen.it/download/. (Online; accessed 07 February 2023).

[52] ORTEC/AMETEK Oak Ridge, T.N. USA, https://www.ortec-online.com/products/. (Online; accessed 22 September 2022).

[53] MIDAS - Multi Instance Data Acquisition System, http://npg.dl.ac.uk/MIDAS/. (Online; accessed 22 February 2023).

[54] A. State, S. Beck, D. Amanbayev, D. Balabanski, H. Brand, P. Constantin, T. Dickel, C. Hornung, D. Nichita, W. Plaß, H. Roesch, A. Rotaru, C. Scheidenberger, J. Siebring, A. Spataru, N. Tortorelli, J. Zhao, The slow control system of the FRS Ion Catcher, Nucl. Instrum. Methods Phys. Res. A 1034 (2022) 166772, http://dx.doi.org/10.1016/j.nima.2022.166772.

[55] Quantar Technology Inc., http://www.quantar.com/pages/qtihome.htm. (Online; accessed 23 July 2023).

[56] L. Grassi, J. Forneris, D. Torresi, L. Acosta, A. Di Pietro, P. Figuera, M. Fisichella, V. Grilj, M. Jakšić, M. Lattuada, T. Mijatović, M. Milin, L. Prepolec, N. Skukan, N. Soić, V. Tokić, M. Uroić, Study of the inter-strip gap effects on the response of double sided silicon strip detectors using proton microbeams, Nucl. Instrum. Methods Phys. Res. A 767 (2014) 99–111, http://dx.doi.org/10.1016/j.nima.2014.08.009, URL https://www.sciencedirect.com/science/article/pii/S0168900214009292.

[57] D. Torresi, D. Stanko, A. Di Pietro, P. Figuera, M. Fisichella, M. Lattuada, M. Milin, A. Musumarra, M. Pellegriti, V. Scuderi, E. Strano, M. Zadro, Influence of the interstrip gap on the response and the efficiency of double sided silicon strip detectors, Nucl. Instrum. Methods Phys. Res. A 713 (2013) 11–18, http://dx.doi.org/10.1016/j.nima.2013.02.027, URL https://www.sciencedirect.com/science/article/pii/S0168900213002155.

[58] D. Torresi, J. Forneris, L. Grassi, L. Acosta, A. Di Pietro, P. Figuera, L. Grilj, M. Jaksić, M. Lattuada, T. Mijatović, M. Milin, L. Prepolec, N. Skukan, N. Soić, D. Stanko, V. Tokić, M. Uroić, M. Zadro, Study of interstrip gap effects and efficiency for full energy detection of double sided silicon strip detectors, J. Phys. Conf. Ser. 590 (2015) 012029, http://dx.doi.org/10.1088/1742-6596/590/1/012029.

[59] J. Yorkston, A. Shotter, D. Syme, G. Huxtable, Interstrip surface effects in oxide passivated ion-implanted silicon strip detectors, Nucl. Instrum. Methods Phys. Res. A 262 (2) (1987) 353–358, http://dx.doi.org/10.1016/0168-9002(87)90873-4, URL https://www.sciencedirect.com/science/article/pii/0168900287908734.

[60] J. Duenas, D. Mengoni, M. Assie, B. Le Crom, A. Sánchez Benítez, B. Genolini, Y. Blumenfeld, S. Ancelin, N. de Séréville, T. Faul, F. Hammache, A. Jallat, V. Le Ven, E. Rauly, D. Suzuki, D. Beaumel, I. Martel, Interstrip effects influence on the particle identification of highly segmented silicon strip detector in a nuclear reaction scenario, Nucl. Instrum. Methods Phys. Res. A 743 (2014) 44–50, http://dx.doi.org/10.1016/j.nima.2014.01.009, URL https://www.sciencedirect.com/science/article/pii/S0168900214000175.

[61] G. Cavalleri, E. Gatti, G. Fabri, V. Svelto, Extension of Ramo's theorem as applied to induced charge in semiconductor detectors, Nucl. Instrum. Methods 92 (1) (1971) 137–140, http://dx.doi.org/10.1016/0029-554X(71)90235-7, URL https://www.sciencedirect.com/science/article/pii/0029554X71902357.

[62] E. Vittone, Theory of ion beam induced charge measurement in semiconductor devices based on the Gunn's theorem, Nucl. Instrum. Methods Phys. Res. B 219–220 (2004) 1043–1050, http://dx.doi.org/10.1016/j.nimb.2004.01.210, Proceedings of the Sixteenth International Conference on Ion Beam Analysis. URL https://www.sciencedirect.com/science/article/pii/S0168583X04002605.

[63] M. Reese, J. Gerl, P. Golubev, N. Pietralla, Automatic intrinsic calibration of double-sided silicon strip detectors, Nucl. Instrum. Methods Phys. Res. A 779 (2015) 63–68, http://dx.doi.org/10.1016/j.nima.2015.01.032, URL https://www.sciencedirect.com/science/article/pii/S0168900215000637.

[64] J. Perriére, Rutherford backscattering spectrometry, Vacuum 37 (5) (1987) 429–432, http://dx.doi.org/10.1016/0042-207X(87)90327-7, URL https://www.sciencedirect.com/science/article/pii/0042207X87903277.